# In Search of the Active Sites for the Selective Catalytic Reduction on Tungsten-Doped Vanadia Monolayer Catalysts supported by $TiO_2$

Mengru Li,[†] Sung Sakong,[†] and Axel Groß[*,†,‡]

[†]*Institute of Theoretical Chemistry, Ulm University, 89069 Ulm, Germany*

[‡]*Helmholtz Institute Ulm (HIU), Electrochemical Energy Storage, 89069 Ulm, Germany*

E-mail: Axel.Gross@uni-ulm.de

**Abstract**

Tungsten-doped vanadia-based catalysts supported on anatase $TiO_2$ are used to reduce hazardous NO emissions through the selective catalytic reduction of ammonia, but their exact atomistic structure is still largely unknown. In this computational study, the atomistic structure of mixed tungsta-vanadia monolayers on $TiO_2$ support under typical operating conditions has been addressed by periodic density functional theory calculations. The chemical environment has been taken into account in a grand-canonical approach. We evaluate the stable catalyst structures as a function of the oxygen chemical potential and vanadium and tungsten concentrations. Thus we determine structural motifs of tungsta-vanadia/$TiO_2$ catalysts that are stable under operating conditions. Furthermore, we identify active sites that promise high catalytic activity for the selective catalytic reduction by ammonia. Our calculations reveal the critical role of the stoichiometry of the tungsta-vanadia layers with respect to their catalytic activity in the selective catalytic reduction.

# Keywords

Vanadium-based catalyst; Density functional theory; Selective Catalytic Reduction; stoichiometry; chemical potential


# Introduction

Nitrogen oxide ($NO_x$) emission from various stationary and mobile sources is significantly contributing to air pollution and causing, among others, ozone depletion, smog, acid rain, eutrophication, and eventually global warming.[1,2] Typically $NO_x$ consists of a mixture of NO (95%) and $NO_2$ (5%), and thus efforts of catalytic removal of nitrogen oxide have been focusing on reducing NO emission at low costs and high industrial efficiency.[3] In particular the selective catalytic reduction (SCR) of NO to $N_2$ by ammonia (SCR-$NH_3$: $4NO+4NH_3+O_2 \rightarrow 4N_2+6H_2O$) is widely adopted in industry, acting as an effective $NO_x$ reduction mechanism.[4–6] Commercial catalysts for the SCR-$NH_3$ reaction consist of W-doped $V_2O_5$ supported on anatase $TiO_2$.[6] Vanadia has been identified as the catalytically active component, while tungsta acts as a promoter to increase the activity and thermal stability.[7]

In spite of its excellent efficiency, vanadium-based SCR catalyst still face several drawbacks: (a) low $N_2$ selectivity at high temperature due to $N_2O$ formation; (b) high conversion rate of $SO_2$ into $SO_3$ in the flue gas which will deactivate the catalyst; (c) phase transformation of anatase $TiO_2$ into inactive rutile above 500°C; (d) narrow operating window between 300 to 400°C.[4,8] Therefore, a further improvement of SCR catalysts is urgently required in order to boost their performance.

In practice, the optimization of the vanadium loading plays an essential role in obtaining a high SCR activity. With increasing vanadium loading below the amount corresponding to monolayer $V_2O_5$, isolated and distorted tetrahedral vanadium oxides separated by tungsten oxide regions transform into catalytically more active oligomeric or polymeric metavanadate species that lead to a higher performance of the catalyst.[9–14] However, once crystalline $V_2O_5$

thin films form at high loading, the SCR activity steeply decreases.[9,10,15,16] Therefore, any strategy to design an improved catalyst needs to focus on optimal vanadium loading to provide active and stable vanadium oligomer configurations. Thus, identifying the active site of the monolayer $W_xV_yO_z/TiO_2$ catalyst, understanding the role of the W doping, and designing stable and active catalyst structures based on microscopic insights will be essential for the systematic improvement of performance and thermal stability in the spirit of obtaining fundamental and conceptual insights into catalytic phenomena.[17]

First-principles electronic structure calculations based on density functional theory (DFT) allow the microscopic assessment of the properties of catalysts ,[18–28] and together with grand-canonical schemes[23,28] also an assessment of their energetic stability under operating conditions. Numerous experiments studying the catalytic activity of surface vanadium oxides[29–31] stressed the specific role of dangling oxygen atoms on the active $VO_x$ surfaces. However, to the best of our knowledge, most theoretical studies addressing the SCR have modeled the active catalyst as a $VO_3H$ monomer supported on $TiO_2$[32–37] or as clean unsupported $V_2O_5$.[38–40] In addition, $V_2O_7$ clusters have also been employed as model catalysts to represent polymeric vanadyl species.[34,41,42] Thus, it is an open question whether the model catalysts used in these theoretical studies fully capture the properties of the complex catalysts used in the industry and identify the correct active sites. Hence as the first step in any atomistic study addressing the properties of catalysts, it is in principle mandatory to scrutinize whether the considered structures entering the modeling are realistic and stable under operating conditions ,[23–25,27] in particular considering the fact that the structure of nano-sized catalyst can be rather dynamic under operating conditions.[43,44]

Here we follow precisely this approach in the computational search for catalyst structures active in the selective catalytic reduction. In this search, we will focus on stable structural motifs promising high SCR activity as a function of the tungsten and vanadium loading. Note that the nature of the catalytically active site on vanadia-based catalysts has been controversially discussed for a long time, with both Lewis and Brønsted acid sites being

proposed.[6,29,32,36,41,45–47] However, recently infrared spectroscopic studies[46,47] have indicated that, in particular, Lewis acid sites are crucial for the SCR activity whereas Brønsted acid sites contribute to a lesser extent. Furthermore, according to DFT calculations, strong Brønsted acidity has been found to be disadvantageous for the SCR activity.[32] However, no clear picture of the active site has been evolved yet. At least there appears to be a consensus that vanadyl (V=O) species play a crucial role in the SCR.[41,46] Yet, the acidity of the active sites can be influenced by dopants in the oxide layer.[32] Hence it is not sufficient to consider only local oxide motifs in the determination of the SCR activity. Rather, the support and a realistic catalyst structure need to be included in the assessment of the catalytic activity.

Therefore we will first tailor $W_xV_yO_z/TiO_2$ catalysts by varying their vanadium, tungsten, and oxygen concentrations and distributions and then determine their thermodynamic stability under operating conditions using a grand-canonical approach.[23] We will then analyze the resulting stable structures in terms of their potential catalytic activity by identifying motifs in these structures that promise a high SCR activity. We will show that the stoichiometry of the tungsta-vanadia layers is a critical factor influencing their reactivity. By controlling the acidity through the catalyst composition, we will propose a general strategy for designing stable and active SCR catalysts.

# Computational details

Spin-polarized periodical first-principles calculations based on density functional theory (DFT) were performed using the VASP software[48–50] with the projected augmented wave (PAW) method.[51,52] Exchange-correlation effects were considered within the generalized gradient approximation (GGA) using the Perdew-Burke-Ernzerhof (PBE) functional.[53] The wave functions were expanded by a plane wave basis with a kinetic cut-off energy of 400 eV. On-site Coulomb interactions were taking into account through the DFT+U approach[54,55] to treat the highly localized Ti 3d states in $TiO_2$, using a parameter of $U - J = 3.5$ eV.[56]

Dispersion effects were treated based on the DFT-D3 method.[57]

For the bulk optimization of $TiO_2$, $V_2O_5$, and $WO_3$, a k-point mesh[58] of $9 \times 9 \times 9$ was applied to integrate over the first Brillouin zone. All atoms were allowed to relax during the bulk calculations. The calculations were considered to be converged when the forces on each atom were smaller than $0.001\,\mathrm{eV/\AA}$. At room temperature, the most stable $WO_3$ structure is the $\gamma$-monoclinic phase. We obtained optimized lattice constants of $a = 7.30$ Å, $b = 7.53$ Å, and $c = 7.68$ Å for this structure. Anatase $TiO_2$ was selected as the support for the SCR catalyst with an optimized lattice constant of 3.83 Å. The lattice parameters of $\alpha$-$V_2O_5$, the most stable phase of the vanadium oxide at room temperature, turned out to be $a = 11.49$ Å, $b = 4.44$ Å, and $c = 3.59$ Å, respectively. The cohesive energy, the heat of formation, and the M-O distances for the three considered bulk materials are collected in Tab. 1, where the cohesive energy has been normalized to the number of metal atoms in the primitive unit cell, and the heat for formation was calculated as the energy cost of oxidizing the reduced phases Ti, $VO_2$, and $WO_2$ into $TiO_2$, $V_2O_5$, and $WO_3$, respectively, by gas-phase $O_2$ under the standard condition.

The support was modeled by low-index $TiO_2$ surfaces with (001), (100), and (101) terminations. In addition, a well-known admolecule (ADM) surface reconstruction[59] was taken into account for $TiO_2$(001). The symmetric slabs consisting of eight atomic layers were used, and all atoms in the slabs were fully relaxed. The surface structures were assumed to reach convergence when forces on each atom were smaller than 0.03 eV/Å. We have tested the convergence using $3 \times 3 \times 1$ and $5 \times 5 \times 1$ meshes and found that the energy change was negligible. Therefore, we employed a $3 \times 3 \times 1$ k-point mesh for the slab calculations. A

Table 1: The cohesive energy ($E_{\mathrm{coh}}$), heat of formation ($\Delta H_f$), and M-O distances ($d_{\mathrm{M-O}}$) for each metal element (M=Ti,V,W) in the unit cell.

| | $TiO_2$ | $V_2O_5$ | $WO_3$ |
|---|---|---|---|
| $E_{\mathrm{coh}}$ (eV) | $-22.41$ | $-22.37$ | $-28.03$ |
| $\Delta H_f$ (eV) | 8.50 | 6.50 | 11.20 |
| $d_{\mathrm{M-O}}$ (Å) | 1.95 | $1.79, 1.89, 1.61$ | 1.92 |

dipole correction was included to compensate for the interaction between surface dipoles and their periodic images. A vacuum layer of 25 Å was chosen to separate the slabs to avoid any spurious interactions normal to the surface.

The $W_xV_yO_z$ layer structures were derived from the corresponding unit cells of low-index surfaces of $WO_3$ and $V_2O_5$. The $W_xO_z$ layers were constructed from the most stable surfaces,[60] ($\sqrt{2} \times \sqrt{2}$) R45°-reconstructed $WO_3(001)$ and $WO_3(001)$. $V_2O_5(010)$, (001), and (100) were chosen as candidate structures for the $V_xO_y$ monolayer. Through substituting V by W and adjusting the oxygen coordination number, $W_xV_yO_z$ layers were created. Afterward these $W_xV_yO_z$ layers were placed onto stable $TiO_2$ surfaces, i.e., ADM-$TiO_2(001)$ and $TiO_2(001)$, where the bottom layer of the $TiO_2$ slab was kept fixed at the bulk configuration. In this way, monolayer-$W_xV_yO_z/TiO_2$ catalysts were tailored.

It is important to realize that the stability of non-stoichiometric surfaces always depends on the environment representing the corresponding reservoirs. To describe the relative energetics of the support, including V and W loading under experimental conditions, we evaluate the surface energy $\gamma(T, p)$ at temperature $T$ and pressure $p$ within the grand-canonical ab initio thermodynamics scheme:[23]

$$\gamma(T,p) = \frac{1}{2A}\left[G(T,p,N_{\mathrm{Ti}},N_{\mathrm{V}},N_{\mathrm{W}},N_{\mathrm{O}}) - \sum_{\mathrm{i}} N_{\mathrm{i}}\mu_{\mathrm{i}}\right], \tag{1}$$

where $A$, $G$ are the surface area and the Gibbs free energy of a configuration consisting of $N_i$ atoms where $i$ stands for Ti, V, W, and O atoms. $\mu_i$ represents the chemical potential of each species $i$. We suppose that the bulk phase of $TiO_2$ is in thermodynamic equilibrium with gas-phase $O_2$ under specific conditions. Hence the Ti chemical potential is $\mu_{\mathrm{Ti}} = \mu_{\mathrm{TiO_2}}^{(bulk)} - 2\mu_{\mathrm{O}}$, with the Gibbs free energy of bulk $TiO_2$ ($\mu_{\mathrm{TiO_2}}^{(bulk)}$). The chemical potential of oxygen $\mu_{\mathrm{O}}(T, p)$ can be expressed as

$$\mu_{\mathrm{O}}(T,p) = \frac{1}{2}\left[\mu_{\mathrm{O_2}}(T,p^{\Theta}) + RT\ln(p_{\mathrm{O_2}}/p^{\Theta})\right], \tag{2}$$

where $\mu_{O_2}(T, p^{\Theta})$ is the energy of dioxygen gas at temperature $T$ and standard atmospheric pressure $p^{\Theta}$. The temperature dependence of $\mu_{O_2}(T, p^{\Theta})$ has been taken from the NIST-JANAF thermodynamic Table.[61] $p_{O_2}$ is the partial pressure of oxygen gas. We identify the O-rich limit of $\mu_{O_2}$ with gas-phase $O_2$ under the standard conditions and the O-poor limit with the formation of bulk $TiO_2$ from metallic Ti, i.e., the heat of formation is $-\Delta H_f = \mu_{TiO_2}^{(bulk)} - \mu_{Ti}^{(bulk)} - \mu_O$.

The chemical potential of vanadium refers to the bulk phase $V_2O_5$, i.e., $\mu_V = (\mu_{V_2O_5}^{(bulk)} - 5\mu_O)/2$. Here, the O-poor limit corresponds to the $VO_2$ formation. Then, $\mu_O$ satisfies $\mu_{V_2O_5}^{(bulk)} - 2\mu_{VO_2}^{(bulk)} = -6.50$ eV for $VO_2$ formation. Since the O-poor limit for the $VO_2$ formation is within the range of $TiO_2$ formation, we assign the O-poor limit to the heat of formation of $VO_2$ for $V_xO_y/TiO_2$. We assume the chemical potential of W to be in equilibrium with the bulk phase $WO_3$, i.e., $\mu_W = \mu_{WO_3}^{(bulk)} - 3\mu_O$. The O-poor limit refers to oxygen chemical potential for $WO_2$ formation, $\mu_{WO_3}^{(bulk)} - \mu_{WO_2}^{(bulk)} = -11.20$ eV. As the limit of $\mu_O$ for $WO_2$ and metallic Ti formation is beyond the range allowing $VO_2$ formation, the O-poor limit for $W_xO_yO_z/TiO_2$ is given by the one for $VO_2$ formation.

## Modeling $TiO_2$-supported Monolayer $V_2O_5$-$WO_3$ Catalysts

Since only catalyst configurations that are energetically stable under operating conditions promise longevity and thermal stability, we will search for energetically stable catalyst layers but also try to assess their activity. Firstly we will screen the $TiO_2$ support among the low-index (001), (010), and (100) terminations. Then the energetics of $V_yO_z$ layers on selected $TiO_2$ supports based on structural motifs of $V_2O_5$(001), (010), and (100) facets will be discussed in order to probe energetically favorable $V_2O_5/TiO_2$ configurations. On the basis of the most stable $V_2O_5/TiO_2$ configurations, different amounts of vanadium atoms will be substituted by tungsten to model tungsten loading effects. The coordination of the involved oxygen atoms will be adjusted to achieve higher stability. In this way, a systematic map of

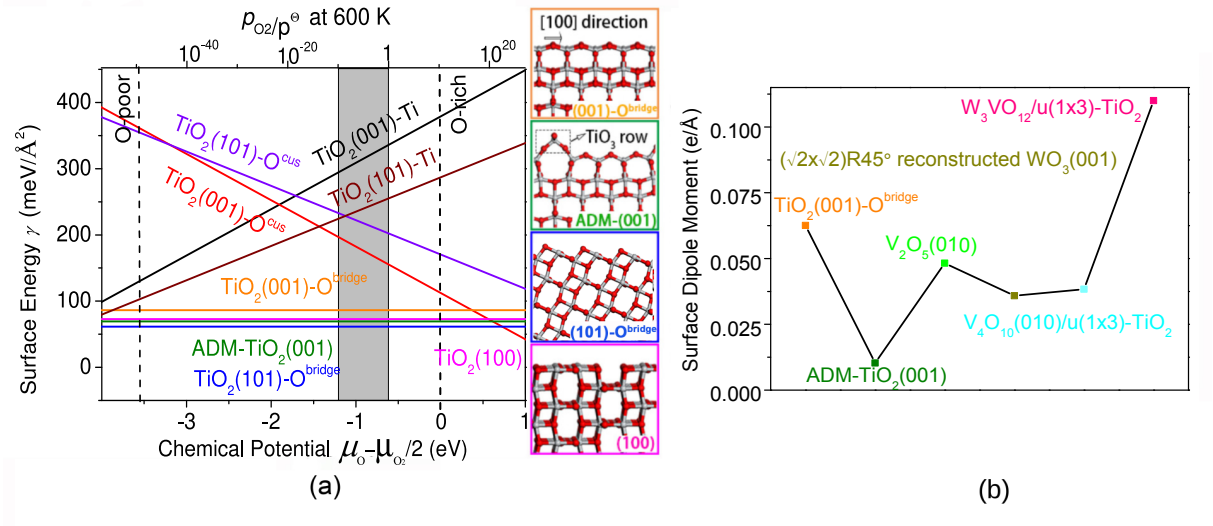


Figure 1: Calculated properties of $TiO_2$(001), (100), and (101) surfaces. a) Surface energies of various terminations as a function of the oxygen chemical potential. The grey shadowed area refers to the experimental growth condition of the catalyst; b) Surface dipole moment per area for various catalyst layers. Selected structures are illustrated as side views. The O and Ti atoms are colored in red and grey, respectively.

stable $TiO_2$,$V_2O_5$/$TiO_2$ and $V_2O_5$-$WO_3$/$TiO_2$ catalysts is constructed.

## Screening $TiO_2$ supports

The support is modeled by $TiO_2$(001) and (101) surfaces with various terminations. We consider O termination at the bridge site (-$O^{bridge}$), Ti termination (-Ti), and O termination at the top site (-$O^{cus}$). To model the reconstructed $TiO_2$(001) surface, as shown in Fig. 1, we adapted the admolecule (ADM) model as proposed by Lazzeri and Selloni, [59] i.e., a (1×4) unit cell was used. In this reconstruction, one row of surface oxygen atoms is replaced by one row of $TiO_3$ units. The surface energies of $TiO_2$ with different terminations are shown in Fig. 1a. Experimental conditions are indicated by the gray box in Fig. 1. This area corresponds to the operating window of oxygen pressure within atmospheric pressure at 600 K. [62]

We find that the stoichiometric $TiO_2$(101)-$O^{bridge}$, $TiO_2$(100), $TiO_2$(001)-$O^{bridge}$, and the $TiO_2$(001)-(1 × 4)-ADM reconstructed surfaces (blue, pink, yellow and green lines in Fig. 1a, respectively) are the most stable under the preparation conditions of the catalyst. We note

that the presented surface energies are in general lower than previously reported values[63] which we attribute to the additionally considered van der Waals interactions.

The most stable $TiO_2$(101)-$O^{bridge}$ surface termination is known for its weak interaction with adsorbates such as vanadium species due to the fact that it exposed sixfold fully coordinated Ti atoms.[63,64] Therefore, we do not consider it in the following anymore. Furthermore, the uneven distribution of Ti atoms on the $TiO_2$(100) surface disfavors the deposition of vanadium oxide so that it is hard to grow the vanadium oxide on $TiO_2$(100). In contrast, the vanadium oxide can be easily formed on the (001) surface because of the exposed fivefold unsaturated Ti atoms, and the similar geometry of $TiO_2$(001) and vanadium oxide.[42] However, note that $TiO_2$(001) can be further stabilized into the much more stable $(1 \times 4)$-ADM reconstruction.[59] The $TiO_2$(001) surface is a polar surface due to its triple-layer structure. An inward relaxation of the top O atomic layer reduces its large dipole moment yielding rearranged asymmetric Ti-O bonds along the [100] direction. It results in inequivalent bond lengths of neighboring Ti-O bonds along the [100] direction (1.84 Å and 2.11 Å). The $TiO_3$ row makes the surface uneven, but relieves the surface stress,[59] and reduces the surface dipole moment, as Fig. 1b shows. Based on the arguments given above, in the following, we consider both the $TiO_2$(001) and the $TiO_2$(001)-$(1 \times 4)$ reconstructed surface as the support for the SCR catalyst growth.

## Formation of vanadium oxide layers on $TiO_2$(001)

After determining the structure of the $TiO_2$ support, we consider the formation of vanadia layers on this support by screening the stability of $V_yO_z$ layers as a function of the oxygen partial pressure. The initial configurations of the considered layers subject to further relaxation are inspired by the structures of the low-index $V_2O_5$ (010), (001), and (100) surface with an additional variation of the number of vanadium and oxygen atoms. As the reconstruction of the $TiO_2$(001) may be lifted upon the deposition of a $V_xO_y$ layer, we consider both the $TiO_2$(001)-$(1 \times 4)$ reconstructed surface as well as the unreconstructed $TiO_2$(001) surface as

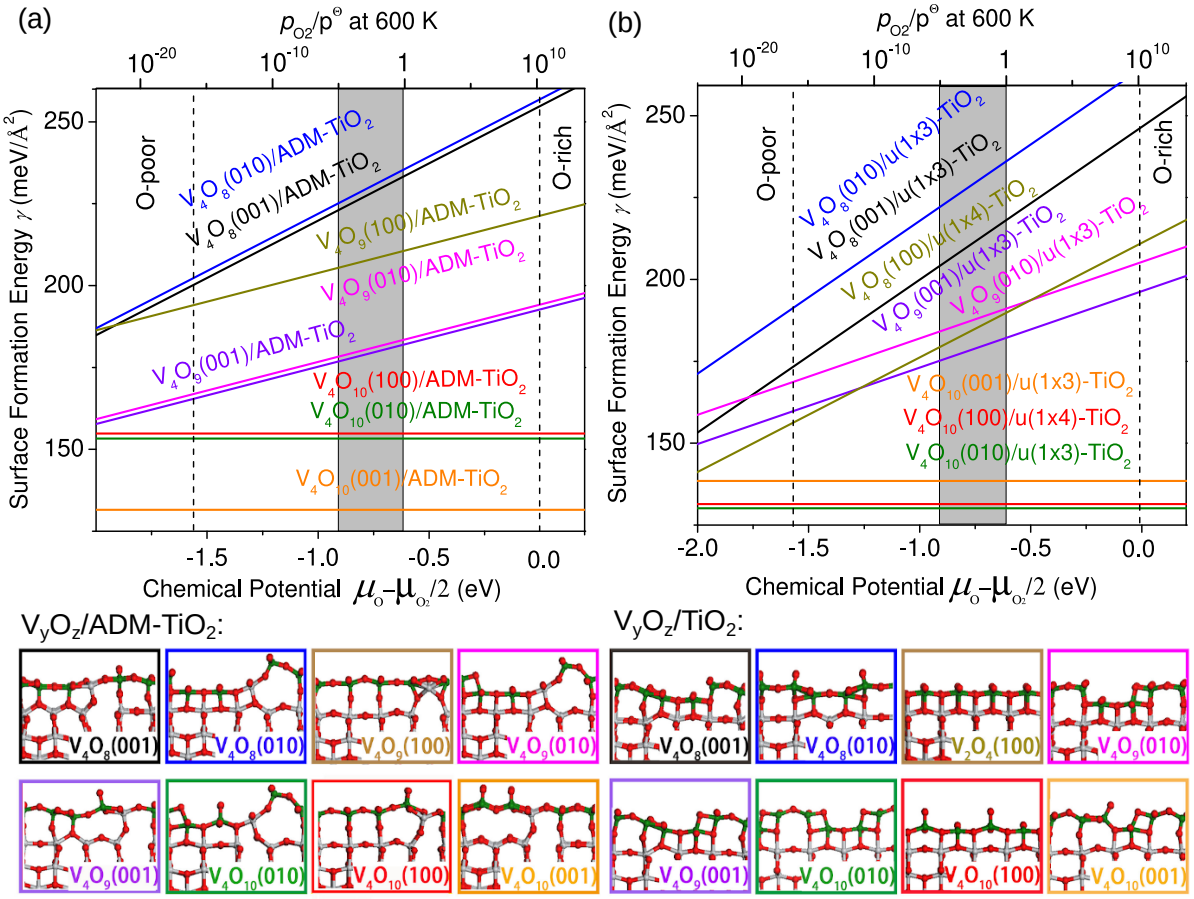


Figure 2: Surface formation energies of $V_yO_z/(1 \times 4)$-ADM reconstructed $TiO_2$ surface (a), $V_yO_z/TiO_2$ surface (b). The grey shadowed area refers to the experimental condition[62] for SCR reaction. In the side views of surface configurations, red, grey, and green colored spheres represent O, Ti, and V atoms, respectively.

the support. Note that the reconstructed $TiO_2(001)$-$(1 \times 4)$ surface consists of $TiO_2(001)$-$(1 \times 3)$ terraces plus the additional protruding $TiO_3$-like rows (see Fig. 1). Therefore we consider $V_yO_z$ layers that fill up the terraces between these $TiO_3$-like rows. Consequently, for the unreconstructed $TiO_2(001)$ surface, we consider $V_yO_z$ layers on $(1 \times 3)$ surface unit cells which have the same $V_yO_z$ "coverage" as the $TiO_2(001)$-$(1 \times 3)$ terraces of the reconstructed surfaces. Furthermore, we also addressed $V_yO_z$ layers on $TiO_2(001)$-$(1 \times 4)$.

The surface energies of $V_yO_z$ layer on the $TiO_2$ support are plotted as a function of the oxygen chemical potential in Fig. 2. First of all, we note that the surface formation energies are all above 130 meV/Å$^2$, which is twice as large as the lowest $TiO_2$ surface energy (see

Fig. 1a). This large difference in surface energy between the $TiO_2$ support and the vanadia-covered support also explains why in the experiment still large fractions of uncovered $TiO_2$ are observed upon vanadium exposure that is nominally sufficient to form a complete vanadia layer.[15] Besides, the most stable surface termination of bulk $V_2O_5$, the $V_2O_5(001)$ surface, has a rather low surface energy of 7.33 meV/Å$^2$ according to our calculations, and the adsorption of the vanadia monolayer onto the $TiO_2$ increases the surface energy by around 44.00 meV/Å$^2$ taking bulk $V_2O_5$ as the reference. Thus, the formation of $V_2O_5$ nanoparticles is favored. This is consistent with the fact that such vanadia nanoparticles have indeed have been found on $TiO_2$,[65] depending on the precursor used in the vanadia overlayer preparation.

Figure 2 demonstrates that the stoichiometric $V_4O_{10}$ layers on both $TiO_2$ and ADM-$TiO_2$ are always the most stable. Note that the surface energies of the stoichiometric surface terminations are represented by flat lines because they do not depend on the chemical potentials of the constituents. In order to get insight into the structure determining factors, we estimate the interaction energy between the $TiO_2$ support and the considered $W_xV_yO_z$ catalyst layers using

$$E^{\mathrm{int}}_{\mathrm{W_xV_yO_z-support}}(T,p) = \gamma(\mathrm{T,p}) - \left(E^{\mathrm{form}}_{\mathrm{support}}(T,p) + E^{\mathrm{form}}_{\mathrm{W_xV_yO_z}}(T,p)\right) \ , \tag{3}$$

where $\gamma(\mathrm{T,p})$ is the surface energy of the whole system, $E_{\mathrm{support}}(T,p)$ and $E_{\mathrm{W_xV_yO_z}}(T,p)$ are the formation energies per surface area of the support and the catalyst layer alone in the frozen configuration of the whole system. As Tab. 2 demonstrates, whereas the breaking of the $TiO_3$ rows upon the formation of the stoichiometric $V_4O_{10}(001)$ layer requires a significant amount of deformation energy (214.93 meV/Å$^2$), the stronger interaction between vanadium species and support leads to an energy gain of 192.40 meV/Å$^2$. Due to these compensating energetic effects of the deformation and the support-vanadia interactions shown in Tab. 2, the stoichiometric $V_4O_{10}(001)$ layer on ADM-$TiO_2$ exhibits a similar stability as the vanadia (010) and (100) layers on unreconstructed $TiO_2$. Even more interesting is

the fact that the stoichiometric $V_4O_{10}(010)$/u(1×3)-$TiO_2$ is slightly more stable than the $V_4O_{10}(100)$/u(1×4)-$TiO_2$. The $V_4O_{10}(010)$/u(1×3)-$TiO_2$ has a $V_2O_5$ coverage that is 1/3 higher than the $V_4O_{10}(100)$/u(1×3)-$TiO_4$. Consequently, its structure looks more open and distorted. Still, as Tab. 2 reveals, obviously its structure is close to the $V_2O_5$ bulk structure because its formation energy with respect to bulk $V_2O_5$ is much lower than those of the $V_4O_{10}(100)$/u(1×4)-$TiO_2$.

## W loading into vanadia catalyst layer

We will now consider the stability of vanadia catalyst layers upon additional exposure to tungsten atoms. Note that due to the different stoichiometry of vanadia and tungsta, $V_2O_5$ vs. $WO_3$, the addition of tungsten atoms also modifies the fact which $W_xV_yO_z$ adlayers are stoichiometric. This offers a larger variability of oxygen-excess and oxygen-deficient configurations dependent on the tungsten loading which also influences the local electronic charge at the vanadium and tungsten atom and thus also their formal oxidation states. Due to the fact that we found several $V_2O_5/TiO_2$ layers with similar surface formation energies, we probed the thermodynamic stability of tungsten substitution into $V_4O_{10}$ layers, i.e., in $V_4O_{10}(001)$/ADM-$TiO_2$ (Fig. 3) and in $V_4O_{10}(010)$/u(1×3)-$TiO_2$ and $V_4O_{10}(100)$/u(1×4)-$TiO_2$ (Fig. 4). In practice, the $W_xV_yO_z$ layers on $TiO_2$ are constructed from the $V_2O_5/TiO_2$ surfaces through substitution of V by W and modifying the number of coordinating oxygen

Table 2: Decomposition of surface formation energy for $W_xV_yO_z/TiO_2$ layer (unit: meV/Å$^2$)

| Model | $E^{form}_{W_xV_yO_z}$ | $E^{form}_{support}$ | $E^{int}_{W_xV_yO_z-support}$ |
|---|---|---|---|
| $V_4O_{10}(001)$/ADM-$TiO_2$ | 109.03 | 214.93 | −192.40 |
| $V_4O_{10}(010)/TiO_2$ | 103.25 | 160.21 | −133.60 |
| $V_4O_{10}(100)/TiO_2$ | 150.56 | 168.64 | −188.81 |
| $WV_3O_{11}$/u(1×3)-$TiO_2$ | 135.49 | 166.08 | −153.20 |
| $WV_3O_{11}$/u(1×4)-$TiO_2$ | 134.84 | 162.55 | −153.78 |
| $W_3V_1O_{12}$/u(1×3)-$TiO_2$ | 135.65 | 167.53 | −148.89 |
| $W_3V_1O_{12}$/u(1×4)-$TiO_2$ | 80.01 | 150.10 | −98.96 |
| $W_4O_{12}$/u(1×3)-$TiO_2$ | 113.89 | 163.86 | −156.00 |
| $WO_3(001)$-O/$TiO_2$ | 58.73 | 143.03 | −89.88 |

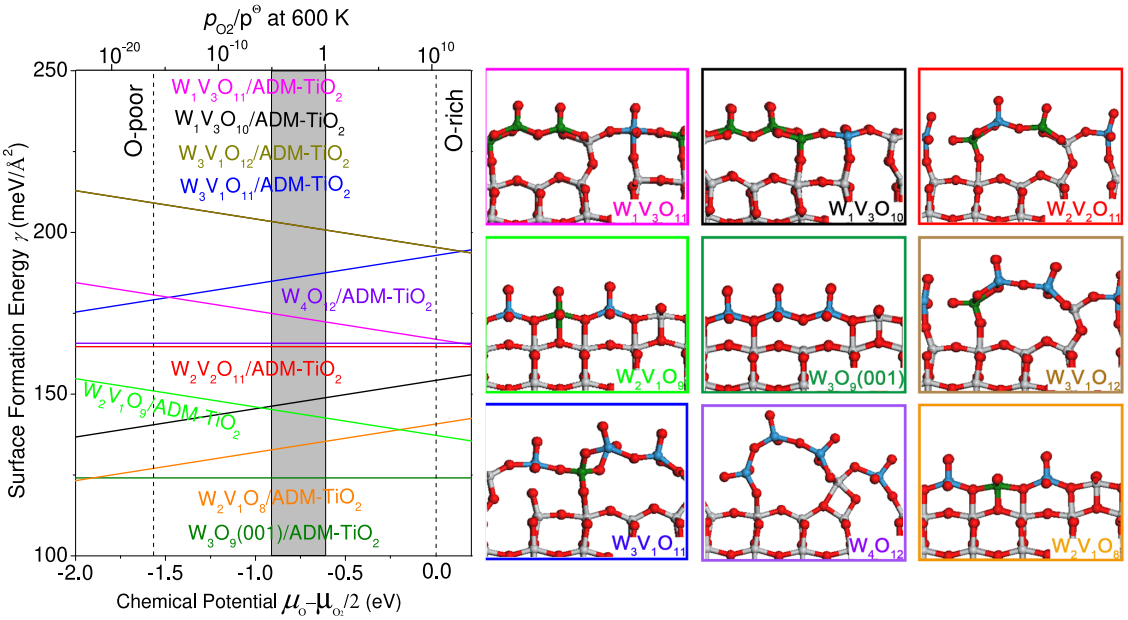


Figure 3: Surface formation energies of W doped $V_4O_{10}(001)/(1 \times 4)$-reconstructed-$TiO_2$, varying surface coverage of W. The grey shadowed area refers to experimental condition[62] range for SCR reaction. In the side views of surface configurations, red, grey, green, and blue colored spheres represent O, Ti, V, W atoms, respectively.

atoms.

On the reconstructed ADM-$TiO_2$ surface, the energetically most favorable $W_3O_9$, $W_2V_1O_9$, and $W_2V_1O_8$ structures (dark green, light green, and orange lines in Fig. 3, the same colors are used to identify the corresponding atomic configurations) are rather compact and flat, the Ti atom is embedded in the surface at about the same height as the V and W atoms. The addition of a metal atom, either W or V, and further oxygen atoms per (1×4) surface unit cell, resulting in $W_1V_3O_{10}$, $W_1V_3O_{11}$, $W_2V_2O_{11}$, $W_3V_1O_{11}$, $W_3V_1O_{12}$, and $W_4O_{12}$ structures, leads to more open and energetically less favorable structures.

Figure 4 displays the surface formation energies and structures of $W_xV_yO_z$ surface layers on the unreconstructed u(1×4)-$TiO_2$ and u(1×3)-$TiO_2$ substrates. These structures have been derived from the most stable $V_4O_{10}(100)$/u(1×4)-$TiO_2$ and $V_4O_{10}(010)$/u(1×3)-$TiO_2$ configurations by tungsten substitution, the variation of the number of oxygen atoms, and subsequent relaxation of the structure. The noticeable change of the W doping is that catalyst layers on the larger (1×4) surface unit cell are smoother than the corresponding

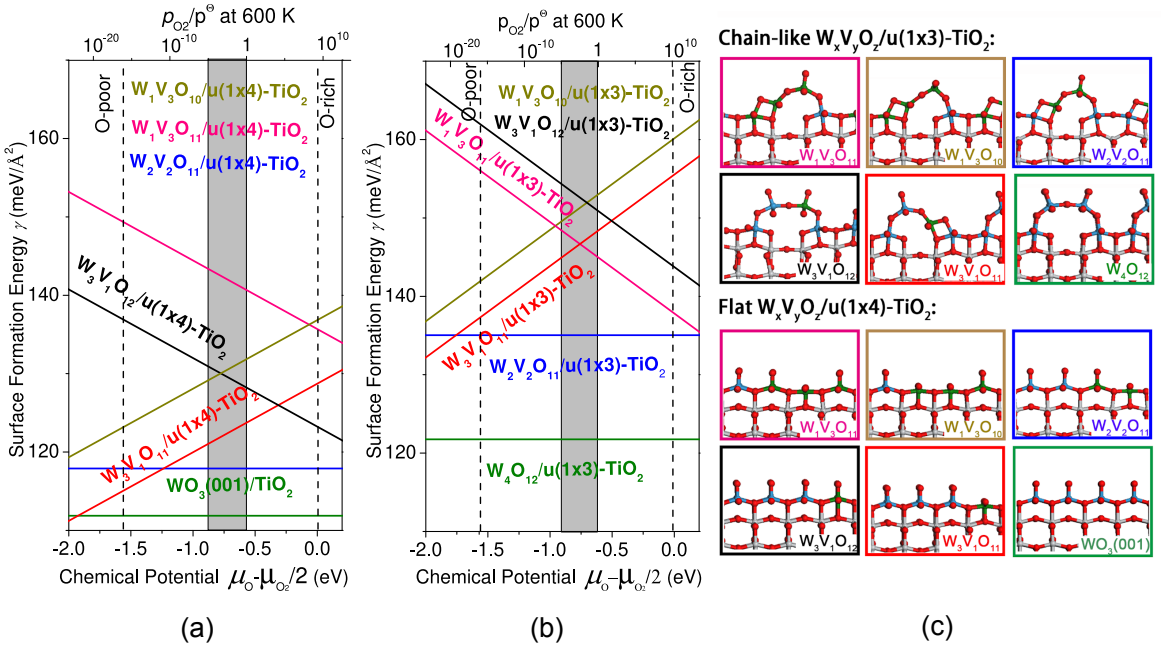


Figure 4: Surface formation energies of W doped $V_4O_{10}(100)$/u(1 × 4)-$TiO_2$ (a) and $V_4O_{10}(010)$/u(1×3)-$TiO_2$ (b) surfaces, varying surface coverage of W, and the corresponding configurations (c). The grey shadowed area refers to experimental condition[62] range for SCR reaction. In the side views, the same color code as in Fig. 3 has been used for the atoms.

ones on the (1×3) surface unit cell where rather open chain-like structures are formed. However, in contrast to the $V_xO_y$ layers on $TiO_2$, now the flat and compact layers on the (1×4) surface unit cell are in general substantially more stable than the open layers on the (1×3) surface unit cell with reduced coordination of some of the metal and oxygen atoms. This might be a consequence of the very similar M-O bond lengths in titanium and tungsten oxide (see Tab. 1), which leads to a smaller lattice misfit between the overlayers and the $TiO_2$ support. This view is supported by the fact that the W-containing overlayers are only modestly deformed, as indicated by the rather small formation energies of the $W_xV_yO_z$ layers of $W_3V_1O_{11}$/u(1×4)-$TiO_2$ and $WO_3(001)/TiO_2$ (see Table 2).

In general, the most stable catalyst layers in both Figs. 3 and 4 correspond to stoichiometric structures, i.e., structures whose surface energy is independent of the oxygen exposure. In comparison to pure vanadia monolayer on the titania support, the most stable stoichiometrc flat $W_2V_2O_{11}$ layer leads to a lowering of the surface energy by about 12 meV/Å$^2$ indica-

tive of a higher thermal stability. This is in good agreement with experimental findings that additional tungsten loading has a stabilizing effect.[66] We associate this promoting role of tungsten on the surface stability again to the better match of the M-O bond lengths in the support and the overlayer which lowers the deformation energy upon the overlayer formation. For the $W_1V_3O_z$ and the $W_3V_1O_z$ surfaces within the (1×4) and (1×3) periodicities, only non-stoichiometric surface compositions are possible. Positive and negative slopes characterize the oxygen-deficient and oxygen-excess layers, in Figs. 3 and 4, respectively.

In the flat surface configurations shown in Fig. 4a, the oxygen-deficient structures are typically more stable than oxygen-excess configurations under the operating conditions (in the grey area). In contrast, under slightly higher oxygen pressure than the operating condition, i.e., the right-hand side of the shadowed area in Fig. 4a, the oxygen-excess structures ($W_3V_1O_{12}$ and $W_1V_3O_{11}$) become energetically comparable with the oxygen-deficient configurations ($W_3V_1O_{11}$ and $W_1V_3O_{10}$).

For the chain-like structure, the $W_1V_3O_{11}$ layers correspond to an interesting case as they have very similar surface formation energies and also a very similar decomposition in the different energy contribution according to Table 2 on both the (1×4) and (1×3)-$TiO_2$ surfaces. For oxygen-rich conditions, the chain-like oxygen-excess $W_1V_3O_{11}$/u(1×3) structure (Fig. 4b) is only slightly less stable than the flat oxygen-excess $W_1V_3O_{11}$/u(1×4)-$TiO_2$ and oxygen-deficient $W_1V_3O_{10}$/u(1×4)-$TiO_2$ structures (see Fig. 4a). In this particular structure, we note that the terminal V=O bond is connected to the $TiO_2$ support through metal-oxygen bonds involving well-coordinated vanadium and tungsten atoms.

## Catalytic activity of $W_xV_yO_z/TiO_2$ structures

In this paper, we mainly focus on the stability of $W_xV_yO_z$ layers on $TiO_2$ support in the active site search for the SCR, as the most active catalyst structure is useless when it is not stable under operating conditions. After discussing the thermodynamic stability of the

$W_xV_yO_z$ surface layers on $TiO_2$, we will still try to estimate their potential catalytic activity. Overall, the $W_xV_yO_z$ layers on the unreconstructed $TiO_2$ support are more stable than the corresponding layers on the ADM-reconstructed $TiO_2$ support. In the following, we will only consider the layers on the unreconstructed support.

We decided to especially consider the presence and properties of the terminal V=O groups in the considered surfaces. Experimental studies have in particular addressed the role of Lewis and Brønsted acid sites in the SCR reaction,[6,29,46,47] but the exact nature and role of these sites in the multi-step SCR reaction could not be resolved entirely in these experimental studies. However, as mentioned above, there appears to be a consensus that the vanadyl (V=O) species play a crucial role in the SCR.[41,46] DFT calculations addressing the SCR reaction on small supported vanadium oxide clusters with monomeric[33,41] and dimeric[41] vanadyl groups came up with slightly different reaction schemes, but they agreed on the crucial role of the V=O group in the dehydrogenation of ammonia through the formation of V-OH. Hence, here we use the hydrogen adsorption energy on the terminal vanadyl groups as a descriptor for the SCR activity as it is directly related to a critical reaction step in the SCR and allows to probe the Lewis acidity of these sites. Note that the initial dehydrogenation of ammonia by an adjacent oxygen atom also plays a crucial role in the ammonia oxidation reaction.[67]

Figure 5 displays the hydrogen adsorption energies on a selected set of $W_xV_yO_z/TiO_2$ structures, i.e., the stoichiometric and non-stoichiometric catalyst layers. The non-stoichiometric structures may include both electron-deficient and electron-excess configurations. However, as H adsorption requires acid sites in the catalytic layer, as we will see below, we only focus on electron-deficient configurations among the non-stoichiometric structures. The hydrogen adsorption energies are referred to the gas-phase water molecule,

$$E_{ads-\mathrm{H}} = E_{\mathrm{H}/catal} - E_{catal} - (\mu_{\mathrm{H_2O}} - \mu_{\mathrm{O_2}}/2)/2 \ , \tag{4}$$

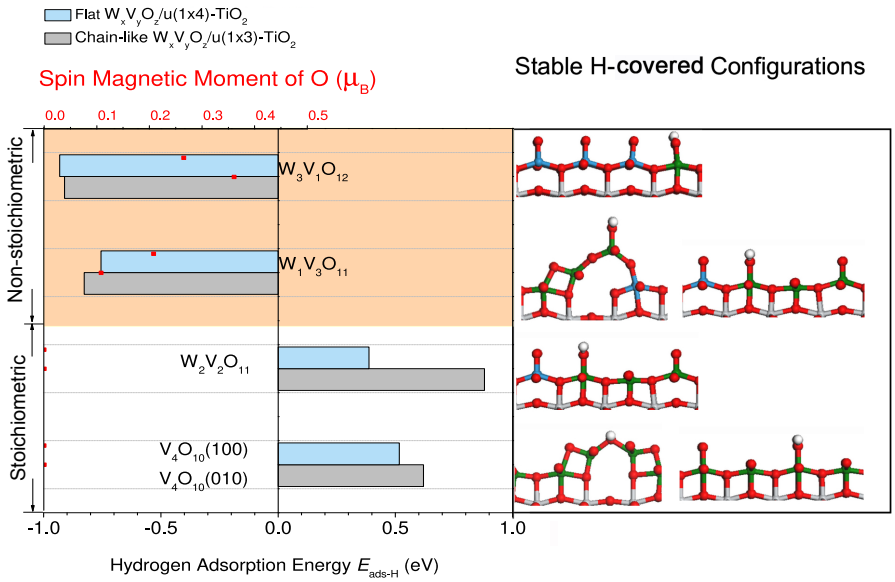


Figure 5: Hydrogen adsorption on selected $W_xV_yO_z/TiO_2$ surfaces. In the left panel, the bars indicate the hydrogen adsorption energies with respect to the water molecule under experimental conditions[62] ($p_{H_2O} = 0.05$ atm and $p_{O_2} = 0.1$ atm at 600 K) and the red dots represent the spin magnetic moment of the active oxygen site. The corresponding hydrogen adsorption configurations are illustrated in the right panel.

where $E_{H/catal}$ and $E_{catal}$ are the energies of the catalyst with/without H adsorption. In practice, the chemical potentials $\mu_{H_2O}$ and $\mu_{O_2}$ have been chosen according to the experimental condition ($p_{H_2O} = 0.05$ atm and $p_{O_2} = 0.1$ atm at 600 K) .[68] Furthermore, we also plot the calculated spin magnetic moment of the oxygen atom (red dots in Fig. 5) of the vanadyl group derived through a charge partitioning scheme[69,70] as an indication of its acidity.

In spite of the supposedly high reactivity of the dangling oxygen atom, it is rather interesting to note that hydrogen adsorption is not energetically favorable with respect to the water molecule on the considered stoichiometric $V_4O_{10}/TiO_2$ and $W_2V_2O_{11}/TiO_2$ catalyst structures shown in Fig. 5. In order to understand the trends in the hydrogen adsorption energies and the electronic factors underlying the hydrogen interaction with the vanadyl groups, we have determined the local $d$-band density of state (DOS) of the V and W atoms neighboring the dangling oxygen of the vanadyl groups and the $p$-band density of states of the dangling oxygen (see Fig. 6), both before and upon hydrogen adsorption.

As far as the non-stoichiometric $W_1V_3O_{11}$ layer is concerned (see Fig. 6a), the partly

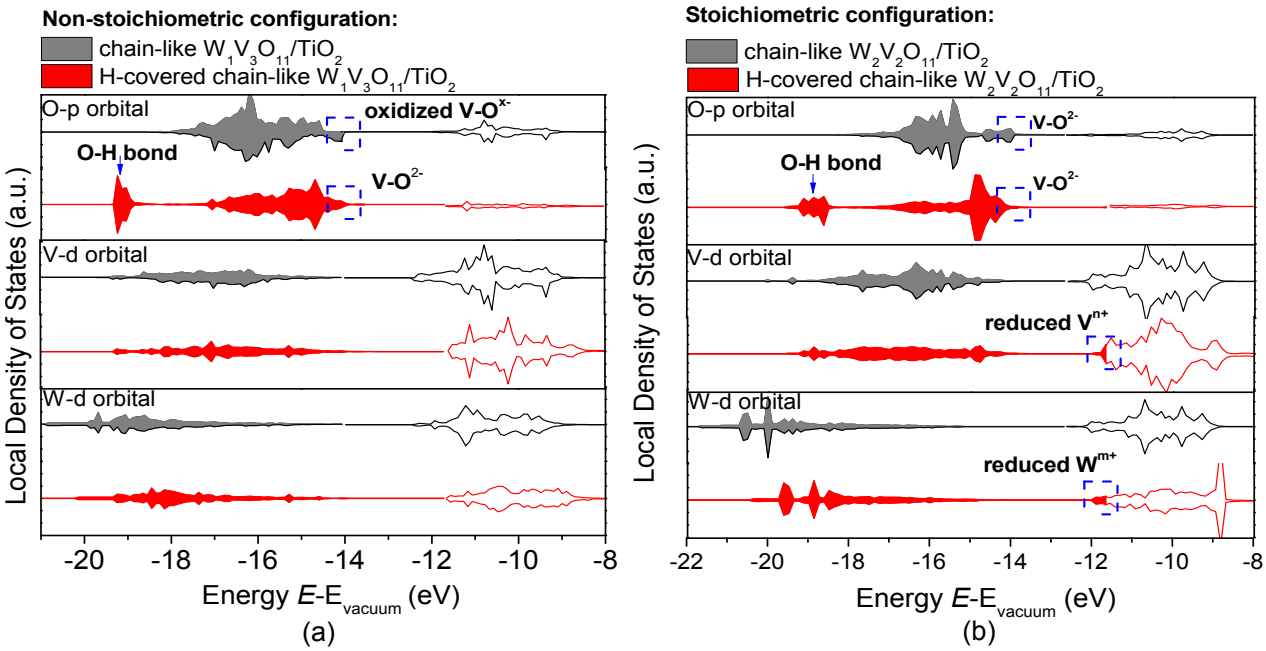


Figure 6: Spin-resolved local $d$-band density of state of the V and W atoms neighboring the dangling oxygen of the vanadyl groups, and $p$-band density of states of the dangling oxygen on (a) $W_1V_3O_{11}/TiO_2$, and (b) $W_2V_2O_{11}$ to the vacuum level, both before and upon hydrogen adsorption. The filled areas highlight the occupied states.

filled $p$-orbitals lead to a non-vanishing spin magnetic moment of the vanadyl oxygen atom, as demonstrated by the asymmetry in the spin-up and spin-down DOS. The same is in fact true for the non-stoichiometric $W_3V_1O_{12}$ layer. An analysis of the local charge distribution indicates that the dominant part of the spin polarization is localized at the vanadyl oxygen site, but it is also somewhat spread out to adjacent sites. We denote the acidity of the vanadyl oxygen by V-$O^{x-}$ with $0 < x < 1$. After H adsorption, the oxygen $p$-orbitals accept electron charge from the hydrogen, and the whole catalyst layer becomes non-magnetic demonstrated by the symmetric spin-up and spin-down DOS in Fig. 6a. We assume that the electron transfer to the catalyst layer saturates all oxygen $p$-states so that the vanadyl oxygen is in the V-$O^{2-}$ state. In fact, upon hydrogen adsorption the catalyst layer becomes stoichiometric with respect to water, tungsta and vanadia. Note that Figs. 3 and 4 demonstrate that the stoichiometric surfaces are energetically much more favored than the non-stoichiometric ones. Thus, the change from non-stoichiometric to stoichiometric configuration stabilizes the

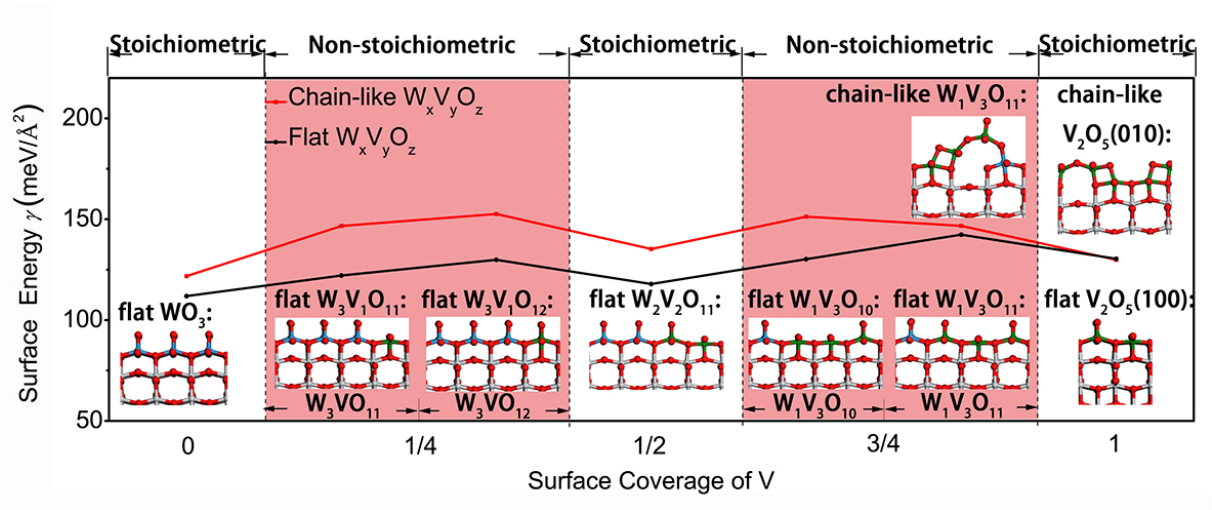


Figure 7: Surface formation energies of $W_xV_yO_z/TiO_2$ catalysts as a function of their $W_xV_y$ composition for $p_{O_2} = 0.1$ atm at 600 K corresponding to a chemical potential $\Delta\mu_O = -0.73$ eV.

catalyst layer significantly which contributes to the energy gain upon hydrogen adsorption.

In contrast, in the stoichiometric $W_2V_2O_{11}$ catalyst layer the dangling oxygen atom can not capture the electron from the adsorbed H atom as it is already fully saturated (see Fig. 6b). Instead, the adsorbed hydrogen atom transfers a large portion of its electron charge to the W and V atoms adjacent to the dangling oxygen. The transferred charge fills the empty $d$ states of the V and W atoms partially, thus leads to a reduction of the $V^{5+}$ and $W^{6+}$ atoms. After hydrogen adsorption, we find spin magnetic moments of 0.19 and 0.10 $\mu_B$ at the V and W sites, respectively. This indicates that both sites capture part of the transferred charge and are reduced to $V^{n+}$ and $W^{m+}$ states with $4 < n < 5$ and $5 < m < 6$. These findings can also be alternatively expressed: hydrogen adsorption on the stoichiometric $W_2V_2O_{11}$ layer leads to a non-stoichiometric $H/W_2V_2O_{11}$ layer with respect to water, tungsta and vanadia which is unstable with respect to the associative desorption of water.

The hydrogen adsorption energies on the stoichiometric and non-stoichiometric catalyst layers shown in Fig. 5 thus directly reflect the electronic state of the terminal vanadyl group and hence also their reactivity with respect to the SCR. On the non-stochiometric surfaces,

the dangling oxygen atoms of the vanadyl group become Lewis acids, i.e., they can accept electrons and thus make hydrogen adsorption favorable. On the other hand, on the stoichiometric surfaces, hydrogen adsorption is not favored, which suppresses the first step in the SCR reaction, the dehydrogenation of ammonia.

From the H adsorption energies on stoichiometric and non-stoichiometric catalysts shown in Fig. 5, we can identify the role of the terminal vanadyl group. When the chemical reactions are related to electron charge transfer to the catalyst, an electron-deficient configuration of the vanadyl group increases the reaction energy by recovering the stoichiometry after the charge transfer. When the V and W atoms play as Lewis acid, the reaction becomes less efficient because of the stoichiometry break. Thus, when the SCR by $NH_3$ is considered, the first step is activated more efficiently by the electron-deficient terminal vanadyl group because the reaction accompanies the charge transfer to the catalyst.

The main results of our work are summarized and showcased in Fig. 7 where the surface energies and the structure of representative $W_xV_yO_z/TiO_2$ catalysts are plotted as a function of increasing vanadium content and characterized with regard to their stoichiometry. It becomes obvious that in general, first, the flat configurations are energetically favorable with respect to the more open chain-like structure, and second, that the stoichiometric configurations are more stable than the non-stoichiometric ones. However, for certain local combinations of the tungsten, vanadium and oxygen content, no stoichiometric surface configurations can form. At these non-stoichiometric surfaces with an oxygen excess, namely the $W_3V_1O_{12}$ and $W_1V_3O_{11}$ surface terminations, unsaturated terminal vanadyl groups can form which act as Lewis acid sites and can thus activate ammonia dehydrogenation. This conclusion is also consistent with the experimental observation of an increased SCR activity under higher oxygen partial pressure.[71] The occurence of these active sites can be hence controlled by tungsten doping.

In addition to the pure reactivity of the dangling oxygen atoms of the terminal vanadyl groups with respect to hydrogen adsorption, one also has to consider the particular ge-

ometry of the environment of the active vanadyl groups. Note that according to previous DFT calculations addressing the SCR reaction on small supported vanadium oxide clusters with monomeric[33,41] and dimeric[41] vanadyl groups, the non-dangling oxygen atoms in the clusters or adjacent Ti sites were instrumental in the adsorption of the $NH_2NO$ reaction intermediates. However, in the flat $W_1V_3O_z$ and $W_3V_1O_z$ layers, the neighboring metal sites are rather far away from the dangling oxygen, and the neighboring non-dangling oxygen atoms are highly coordinated and therefore also inactive. Therefore we suppose that the flat $W_xV_yO_z/TiO_2$ structures are probably less efficient with regard to the SCR reaction. The chain-like $W_1V_3O_{11}/u(1\times3)TiO_2$ surface termination in fact exhibits structural features similar to those considered in the DFT studies of supported vanadium clusters.[33,41] Note also that at this higher vanadium content, the flat and the open chain-like $W_1V_3O_{11}$ configurations are energetically almost degenerate. Hence we consider the open $W_1V_3O_{11}/u(1\times3)TiO_2$ surface termination to be a promising candidate for the active phase of tungsten-doped vanadia SCR catalysts supported on anatase $TiO_2$. Calculations addressing the explicit SCR reaction mechanism on this catalyst are under preparation.

## Surface phase diagram for $WO_3$-$V_2O_5/TiO_2$ catalyst

After having built a large dataset of energetic information about tungsten-doped vanadia monolayer on $TiO_2$ and identified potential active SCR sites, it is essential to analyze the stability of the competing structures with respect to their tungsten and vanadium loading. One could construct the promising structures by just exposing the $TiO_2$ substrate to the "right" amount of tungsten and vanadium atoms. Still, it is also instructive to determine the thermodynamically most stable phases as a function of the chemical potentials of vanadium and tungsten using Eq. 1. The resulting phase diagram for the oxygen-rich limit at a temperature of 600 K is shown in Fig. 8. Within the wide considered range of tungsten and vanadium chemical potentials, only three surface terminations are thermodynamically stable, the flat stoichiometric $WO_3$ and $W_2V_2O_{11}$ and the non-stoichiometric $W_1V_3O_{11}$ surface ter-

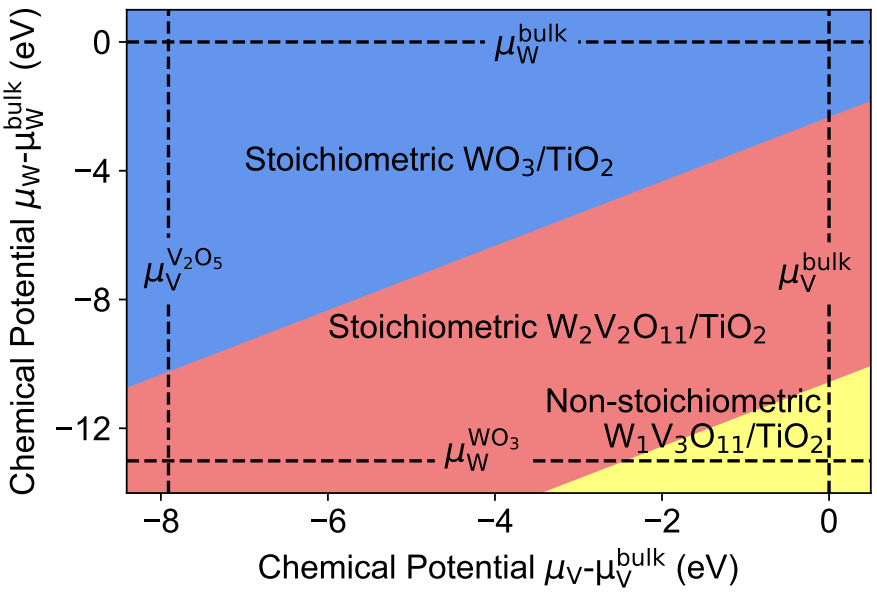


Figure 8: The surface phase diagram of $W_xV_yO_z/TiO_2$ catalyst layers as a function of the vanadium and tungsten chemical potentials for oxygen-rich conditions at a temperature of 600 K.

minations. At high tungsten chemical potentials, only SCR inactive stoichiometric surfaces appear in the phase diagrams. Only at low tungsten chemical potentials and high vanadium chemical potentials, there is a stability pocket for the non-stoichiometric $W_1V_3O_{11}$ surface terminations. Note that the flat and the active chain-like $W_1V_3O_{11}$ surface configuration are energetically almost degenerate (see Fig. 7). Hence both terminations should be present under these stability conditions which we therefore assume to be favorable for a high SCR activity.

## Conclusions

In this first-principles computational study, we have addressed the catalytic activity of tungsten-doped vanadia catalyst monolayers supported on titania with respect to the selective catalytic reduction. We have been guided by the notion that in a theoretical study aimed at obtaining fundamental and conceptual insights into catalytic phenomena, it is critical to first assess the thermodynamic stability of the considered catalytically active

structures. Thus we considered the stability of tungsten vanadium oxide layers supported on titania for varying concentrations of the components using a grand-canonical approach. We find that tungsten doping of the vanadia layers has a twofold role, it improves their stability and allows to tailor the electronic structure to achieve a higher catalytic activity. We showed that the stoichiometric tungsta-vanadia monolayers display a particularly high thermal stability. Using hydrogen adsorption energies as a descriptor for the Lewis acidity, we assessed the potential catalytic activity of the overlayers. It turns out that the stoichiometric tungsta-vanadia monolayers exhibit rather low hydrogen adsorption energies. Instead, non-stoichiometric oxygen-excess surface terminations bind hydrogen more strongly due to the presence of electron-deficient non-saturated terminal vanadyl groups. We also identified an oxygen-excess overlayer structure with low tungsten content that is sufficiently stable to be present under operating conditions and exhibits structural and electronic features that are rather favorable for a high SCR activity. Thus this study provides the basis for a more detailed investigation of the SCR reaction mechanism on tungsten-doped supported vanadia catalysts.

## Acknowledgement

This research has been by the German Research Foundation (DFG) through contract GR 1503/39-1. Support by the Dr. Barbara Mez-Starck Foundation and computer time provided by the state of Baden-Württemberg through bwHPC and the German Research Foundation (DFG) through grant no INST 40/575-1 FUGG (JUSTUS 2 cluster) are gratefully acknowledged. This work contributes to the research performed at CELEST (Center for Electrochemical Energy Storage Ulm-Karlsruhe). Furthermore, the authors thank Xiaoqiang Liu from Sichuan University of Science and Engineering for his kind help in offering computation resources during the shut down of our computer resources caused by a cyber attack.

## Conflict of Interest

The authors declare that the research was conducted in the absence of any commercial or financial relationships that could be constru ed as a potential conflict of interest.

## References


(1) Roy, S.; Hegde, M.; Madras, G. Catalysis for $NO_x$ Abatement. *Appl. Energy* **2009**, *86*, 2283–2297.

(2) Pârvulescu, V.; Grange, P.; Delmon, B. Catalytic Removal of NO. *Catal. Today* **1998**, *46*, 233–316.

(3) Liu, Z.; Woo, S. I. Recent Advances in Catalytic $DeNO_X$ Science and Technology. *Catal. Rev. Sci. Eng.* **2006**, *48*, 43–89.

(4) Busca, G.; Lietti, L.; Ramis, G.; Berti, F. Chemical and Mechanistic Aspects of the Selective Catalytic Reduction of $NO_x$ by Ammonia over Oxide Catalysts: A Review. *Appl. Catal. B* **1998**, *18*, 1–36.

(5) Koebel, M.; Elsener, M.; Kleemann, M. Urea-SCR: a Promising Technique to Reduce $NO_x$ Emissions from Automotive Diesel Engines. *Catal. Today* **2000**, *59*, 335–345.

(6) Han, L.; Cai, S.; Gao, M.; Hasegawa, J.-Y.; Wang, P.; Zhang, J.; Shi, L.; Zhang, D. Selective Catalytic Reduction of $NO_x$ with $NH_3$ by Using Novel Catalysts: State of the Art and Future Prospects. *Chem. Rev.* **2019**, *119*, 10916–10976.

(7) Morikawa, S.; Takahashi, K.; Mogi, J.; Kurita, S. The Effect of the Vanadium Component on the Life of the $WO_3$–$TiO_2$ Catalyst Used for the Reduction of $NO_x$, with $NH_3$. *Bull. Chem. Soc. Jpn.* **1982**, *55*, 2254–2257.

(8) Long, R. Q.; Yang, R. T.; Chang, R. Low Temperature Selective Catalytic Reduction (SCR) of NO with $NH_3$ over Fe–Mn based Catalysts. *Chem. Commun.* **2002**, 452–453.

(9) Went, G. T.; Oyama, S. T.; Bell, A. T. Laser Raman Spectroscopy of Supported Vanadium Oxide Catalysts. *J. Phys. Chem.* **1990**, *94*, 4240–4246.

(10) Vuurman, M. A.; Wachs, I. E.; Hirt, A. M. Structural Determination of Supported Vanadium Pentoxide-Tungsten Trioxide-Titania Catalysts by in Situ Raman Spectroscopy and X-Ray Photoelectron Spectroscopy. *J. Phys. Chem.* **1991**, *95*, 9928–9937.

(11) Eckert, H.; Wachs, I. E. Solid-State Vanadium-51 NMR Structural Studies on Supported Vanadium(V) Oxide Catalysts: Vanadium Oxide Surface Layers on Alumina and Titania Supports. *J. Phys. Chem.* **1989**, *93*, 6796–6805.

(12) Went, G. T.; Leu, L.-J.; Bell, A. T. Quantitative Structural Analysis of Dispersed Vanadia Species in $TiO_2$(Anatase)-Supported $V_2O_5$. *J. Catal.* **1992**, *134*, 479–491.

(13) Kompio, P. G.; Brückner, A.; Hipler, F.; Auer, G.; Löffler, E.; Grünert, W. A New View on the Relations between Tungsten and Vanadium in $V_2O_5$-$WO_3$/$TiO_2$ Catalysts for the Selective Reduction of NO with $NH_3$. *J. Catal.* **2012**, *286*, 237–247.

(14) Kong, M.; Liu, Q.; Jiang, L.; Tong, W.; Yang, J.; Ren, S.; Li, J.; Tian, Y. $K^+$ Deactivation of $V_2O_5$-$WO_3$/$TiO_2$ Catalyst during Selective Catalytic Reduction of NO with $NH_3$: Effect of Vanadium Content. *Chem. Eng. J.* **2019**, *370*, 518–526.

(15) Bond, G. Preparation and Properties of Vanadia/Titania Monolayer Catalysts. *Appl. Catal. A: Gen.* **1997**, *157*, 91–103.

(16) Wachs, I. E. Molecular Structures of Surface Vanadium Oxide Species on Titania Supports. *J. Catal.* **1990**, *124*, 570–573.

(17) Scott, S. L. The Burden of Disproof. *ACS Catal.* **2019**, *9*, 4706–4708.

(18) Sakong, S.; Groß, A. Density functional theory study of the partial oxidation of methanol on copper surfaces. *J. Catal.* **2005**, *231*, 420.

(19) Sakong, S.; Groß, A. The Importance of the Electrochemical Environment in the Electro-Oxidation of Methanol on Pt(111). *ACS Catal.* **2016**, *6*, 5575–5586.

(20) Janssens, T. V. W.; Falsig, H.; Lundegaard, L. F.; Vennestrøm, P. N. R.; Rasmussen, S. B.; Moses, P. G.; Giordanino, F.; Borfecchia, E.; Lomachenko, K. A.; Lamberti, C.; Bordiga, S.; Godiksen, A.; Mossin, S.; Beato, P. A Consistent Reaction Scheme for the Selective Catalytic Reduction of Nitrogen Oxides with Ammonia. *ACS Catal.* **2015**, *5*, 2832–2845.

(21) Li, M.-R.; Wang, G.-C. The mechanism of ethanol steam reforming on the $Co^0$ and $Co^{2+}$ sites: A DFT study. *J. Catal.* **2018**, *365*, 391–404.

(22) Ali, Z.; Wu, Y.-W.; Wu, Y.; Arain, Z.; Xu, M.-X.; Lu, Q.; Ma, H.; Zhao, H.-Y. Inhibition effects of Pb species on the $V_2O_5$-$MoO_3/TiO_2$ catalyst for selective catalytic reduction of $NO_x$ with $NH_3$: A DFT supported experimental study. *Appl. Surf. Sci.* **2020**, *525*, 146582.

(23) Reuter, K.; Scheffler, M. Composition, Structure, and Stability of $RuO_2$(110) as a Function of Oxygen pressure. *Phys. Rev. B* **2001**, *65*, 035406.

(24) Rogal, J.; Reuter, K.; Scheffler, M. CO oxidation at Pd(100): A first-principles constrained thermodynamics study. *Phys. Rev. B* **2007**, *75*, 205433.

(25) Sakong, S.; Groß, A. Total oxidation of methanol on Cu(110): a density functional theory study. *J. Phys. Chem. A* **2007**, *111*, 8814.

(26) Gohda, Y.; Groß, A. Structure–reactivity Relationship for Bimetallic Electrodes: Pt over Layers and PtAu Surface Alloys on Au(111). *J. Electroanal. Chem.* **2007**, *607*, 47–53.

(27) Gossenberger, F.; Juarez, F.; Groß, A. Sulfate, Bisulfate, and Hydrogen Co-adsorption

on Pt(111) and Au(111) in an Electrochemical Environment. *Front. Chem.* **2020**, *8*, 634.

(28) Groß, A. Grand-canonical Approaches to Understand Structures and Processes at Electrochemical Interfaces from an Atomistic Perspective. *Curr. Opin. Electrochem.* **2021**, *27*, 100684.

(29) Tian, H.; Ross, E. I.; Wachs, I. E. Quantitative Determination of the Speciation of Surface Vanadium Oxides and Their Catalytic Activity. *J. Phys. Chem. B* **2006**, *110*, 9593–9600.

(30) Tian, H.; Wachs, I. E.; Briand, L. E. Comparison of UV and Visible Raman Spectroscopy of Bulk Metal Molybdate and Metal Vanadate Catalysts. *J. Phys. Chem. B* **2005**, *109*, 23491–23499.

(31) Wachs, I. E. Catalysis Science of Supported Vanadium Oxide Catalysts. *Dalton Trans.* **2013**, *42*, 11762–11769.

(32) Arnarson, L.; Falsig, H.; Rasmussen, S. B.; Lauritsen, J. V.; Moses, P. G. The Reaction Mechanism for the SCR process on Monomer $V^{5+}$ sites and the Effect of Modified Brønsted Acidity. *Phys. Chem. Chem. Phys.* **2016**, *18*, 17071–17080.

(33) Arnarson, L.; Falsig, H.; Rasmussen, S. B.; Lauritsen, J. V.; Moses, P. G. A complete reaction mechanism for standard and fast selective catalytic reduction of nitrogen oxides on low coverage $VO_x/TiO_2(001)$ catalysts. *J. Catal.* **2017**, *346*, 188–197.

(34) Du, X.; Xue, J.; Wang, X.; Chen, Y.; Ran, J.; Zhang, L. Oxidation of Sulfur Dioxide over $V_2O_5/TiO_2$ Catalyst with Low Vanadium Loading: A Theoretical Study. *J. Phys. Chem. C* **2018**, *122*, 4517–4523.

(35) Wang, X.; Du, X.; Xue, J.; Yang, G.; Chen, Y.; Zhang, L. New Insights into the $N_2O$

Formation Mechanism during Selective Catalytic Reduction of $NO_x$ with $NH_3$ over V-based Catalyst. *Catal. Today* **2020**, *355*, 555–562.

(36) Arnarson, L.; Rasmussen, S. B.; Falsig, H.; Lauritsen, J. V.; Moses, P. G. Coexistence of Square Pyramidal Structures of Oxo Vanadium (+5) and (+4) Species Over Low-Coverage $VO_X/TiO_2$ (101) and (001) Anatase Catalysts. *J. Phys. Chem. C* **2015**, *119*, 23445–23452.

(37) Song, I.; Lee, J.; Lee, G.; Han, J. W.; Kim, D. H. Chemisorption of $NH_3$ on Monomeric Vanadium Oxide Supported on Anatase $TiO_2$: A Combined DRIFT and DFT Study. *J. Phys. Chem. C* **2018**, *122*, 16674–16682.

(38) Yin, X.; Han, H.; Miyamoto, A. Active Site and Mechanism of the Selective Catalytic Reduction of NO by $NH_3$ over $V_2O_5$: A Periodic First-Principles Study. *Phys. Chem. Chem. Phys.* **2000**, *2*, 4243–4248.

(39) Gruber, M. The Selective Catalytic Reduction of NO by $NH_3$ at Brønsted and Lewis Acid Sites of Vanadium Oxide Surfaces. Ph.D. thesis, 2012.

(40) Yao, H.; Chen, Y.; Zhao, Z.; Wei, Y.; Liu, Z.; Zhai, D.; Liu, B.; Xu, C. Periodic DFT Study on Mechanism of Selective Catalytic Reduction of NO via $NH_3$ and $O_2$ over the $V_2O_5$(001) Surface: Competitive Sites and Pathways. *J. Catal.* **2013**, *305*, 67–75.

(41) He, G.; Lian, Z.; Yu, Y.; Yang, Y.; Liu, K.; Shi, X.; Yan, Z.; Shan, W.; He, H. Polymeric vanadyl Species Determine the Low-temperature Activity of V-based Catalysts for the SCR of $NO_x$ with $NH_3$. *Sci. Adv.* **2018**, *4*, eaau4637.

(42) Vittadini, A.; Casarin, M.; Sambi, M.; Selloni, A. First-Principles Studies of Vanadia-Titania Catalysts: Beyond the Monolayer. *J. Phys. Chem. B* **2005**, *109*, 21766–21771.

(43) Schlögl, R.; Abd Hamid, S. B. Nanocatalysis: Mature Science Revisited or Something Really New? *Angew. Chem. Int. Ed.* **2004**, *43*, 1628–1637.

(44) Behrens, M.; Studt, F.; Kasatkin, I.; Kühl, S.; Hävecker, M.; Abild-Pedersen, F.; Zander, S.; Girgsdies, F.; Kurr, P.; Kniep, B.-L.; Tovar, M.; Fischer, R. W.; Nørskov, J. K.; Schlögl, R. The Active Site of Methanol Synthesis over $Cu/ZnO/Al_2O_3$ Industrial Catalysts. *Science* **2012**, *336*, 893–897.

(45) Marberger, A.; Elsener, M.; Ferri, D.; Kröcher, O. $VO_x$ Surface Coverage Optimization of $V_2O_5/WO_3$-$TiO_2$ SCR Catalysts by Variation of the V Loading and by Aging. *Catalysts* **2015**, *5*, 1704–1720.

(46) Marberger, A.; Ferri, D.; Elsener, M.; Kröcher, O. The Significance of Lewis Acid Sites for the Selective Catalytic Reduction of Nitric Oxide on Vanadium-Based Catalysts. *Angew. Chem. Int. Ed* **2016**, *55*, 11989–11994.

(47) Zhu, M.; Lai, J.-K.; Tumuluri, U.; Wu, Z.; Wachs, I. E. Nature of Active Sites and Surface Intermediates during SCR of NO with $NH_3$ by Supported $V_2O_5$–$WO_3/TiO_2$ Catalysts. *J. Am. Chem. Soc.* **2017**, *139*, 15624–15627.

(48) Kresse, G.; Furthmüller, J. Efficiency of Ab-Initio Total Energy Calculations for Metals and Semiconductors Using a Plane-Wave Basis Set. *Comp. Mater. Sci.* **1996**, *6*, 15–50.

(49) Kresse, G.; Furthmüller, J. Efficient Iterative Schemes for Ab Initio Total-Energy Calculations Using a Plane-Wave Basis Set. *Phys. Rev. B* **1996**, *54*, 11169–11186.

(50) Kresse, G.; Hafner, J. Ab Initio Molecular-Dynamics Simulation of the Liquid-Metal–Amorphous-Semiconductor Transition in Germanium. *Phys. Rev. B* **1994**, *49*, 14251–14269.

(51) Blöchl, P. E. Projector Augmented-Wave Method. *Phys. Rev. B* **1994**, *50*, 17953–17979.

(52) Kresse, G.; Joubert, D. From Ultrasoft Pseudopotentials to the Projector Augmented-Wave Method. *Phys. Rev. B* **1999**, *59*, 1758–1775.

(53) Perdew, J. P.; Burke, K.; Ernzerhof, M. Generalized Gradient Approximation Made Simple. *Phys. Rev. Lett.* **1996**, *77*, 3865–3868.

(54) Dudarev, S. L.; Botton, G. A.; Savrasov, S. Y.; Humphreys, C. J.; Sutton, A. P. Electron-Energy-Loss Spectra and the Structural Stability of Nickel Oxide: An LSDA+U Study. *Phys. Rev. B* **1998**, *57*, 1505–1509.

(55) Wang, L.; Maxisch, T.; Ceder, G. Oxidation Energies of Transition Metal Oxides within the GGA + U Framework. *Phys. Rev. B* **2006**, *73*, 195107.

(56) Peng, Y.; Li, J.; Si, W.; Luo, J.; Wang, Y.; Fu, J.; Li, X.; Crittenden, J.; Hao, J. Deactivation and Regeneration of a Commercial SCR catalyst: Comparison with Alkali Metals and Arsenic. *Appl. Catal. B* **2015**, *168-169*, 195–202.

(57) Grimme, S.; Ehrlich, S.; Goerigk, L. Effect of the Damping Function in Dispersion Corrected Density Functional Theory. *J. Comput. Chem.* **2011**, *32*, 1456–1465.

(58) Monkhorst, H. J.; Pack, J. D. Special Points for Brillouin-Zone Integrations. *Phys. Rev. B* **1976**, *13*, 5188.

(59) Lazzeri, M.; Selloni, A. Stress-Driven Reconstruction of an Oxide Surface: The Anatase $TiO_2$(001)-(1 × 4)Surface. *Phys. Rev. Lett.* **2001**, *87*, 266105.

(60) Li, W.; Da, P.; Zhang, Y.; Wang, Y.; Lin, X.; Gong, X.; Zheng, G. $WO_3$ Nanoflakes for Enhanced Photoelectrochemical Conversion. *ACS Nano* **2014**, *8*, 11770–11777.

(61) NIST-JANAF Thermochemical Tables. `doi:10.18434/t42s31`.

(62) Kleemann, M.; Elsener, M.; Koebel, M.; Wokaun, A. Investigation of the Ammonia Adsorption on Monolithic SCR Catalysts by Transient Response Analysis. *Appl. Catal. B* **2000**, *27*, 231–242.

(63) Vittadini, A.; Casarin, M.; Selloni, A. Chemistry of and on $TiO_2$-Anatase Surfaces by DFT Calculations: a Partial Review. *Theor. Chem. Acc.* **2007**, *117*, 663–671.

(64) Song, L.; Zhang, R.; Zang, S.; He, H.; Su, Y.; Qiu, W.; Sun, X. Activity of Selective Catalytic Reduction of NO over $V_2O_5/TiO_2$ Catalysts preferentially Exposed Anatase {001} and {101} facets. *Catal. Lett.* **2017**, *147*, 934–945.

(65) Carrero, C. A.; Keturakis, C. J.; Orrego, A.; Schomäcker, R.; Wachs, I. E. Anomalous Reactivity of Supported $V_2O_5$ Nanoparticles for Propane Oxidative Dehydrogenation: Influence of the Vanadium Oxide Precursor. *Dalton Trans.* **2013**, *42*, 12644–12653.

(66) He, Y.; Ford, M. E.; Zhu, M.; Liu, Q.; Tumuluri, U.; Wu, Z.; Wachs, I. E. Influence of catalyst synthesis method on selective catalytic reduction (SCR) of NO by $NH_3$ with $V_2O_5$-$WO_3/TiO_2$ catalysts. *Appl. Catal. B* **2016**, *193*, 141–150.

(67) Yang, K.; Liu, J.; Yang, B. Mechanism and Active Species in $NH_3$ Dehydrogenation under an Electrochemical Environment: An Ab Initio Molecular Dynamics Study. *ACS Catal.* **2021**, *11*, 4310–4318.

(68) Kröcher, O.; Devadas, M.; Elsener, M.; Wokaun, A.; Söger, N.; Pfeifer, M.; Demel, Y.; Mussmann, L. Investigation of the Selective Catalytic Reduction of NO by $NH_3$ on Fe-ZSM5 Monolith Catalysts. *Appl. Catal. B* **2006**, *66*, 208–216.

(69) Manz, T. A.; Limas, N. G. Introducing DDEC6 Atomic Population Analysis: Part 1. Charge Partitioning Theory and Methodology. *RSC Adv.* **2016**, *6*, 47771–47801.

(70) Limas, N. G.; Manz, T. A. Introducing DDEC6 Atomic Population Analysis: Part 2. Computed Results for a Wide Range of Periodic and Nonperiodic Materials. *RSC Adv.* **2016**, *6*, 45727–45747.

(71) Djerad, S.; Crocoll, M.; Kureti, S.; Tifouti, L.; Weisweiler, W. Effect of Oxygen Concentration on the $NO_x$ Reduction with Ammonia over $V_2O_5$–$WO_3/TiO_2$ Catalyst. *Catal. Today* **2006**, *113*, 208–214.